26379388, Q. Downloaded from https://onlinelibrary.viley.com/doi/10.1002/eyey2.777 by Egyptian National Sti. Network (Ensinet). Wiley Online Library on [1203,2023], See the Terms and Conditions (https://onlinelibrary.viley.com/rerns-and-conditions) on Wiley Online Library for rules of use; OA articles are governed by the applicable Creative Commons Licens

RESEARCH ARTICLE

Air-condition process for scalable fabrication of CdS/ZnS 1D/2D heterojunctions toward efficient and stable photocatalytic hydrogen production

Dongdong Zhang^{1,2} | Jie Teng¹ | Hongli Yang² | Zhi Fang² | Kai Song² | Lin Wang² | Huilin Hou² | Xianlu Lu^{1,2} | Chris R. Bowen³ | Weiyou Yang²

¹College of Materials Science and Engineering, Hunan University, Changsha, People's Republic of China ²Institute of Micro/Nano Materials and Devices, Ningbo University of Technology, Ningbo, Zhejiang, People's Republic of China

³Department of Mechanical Engineering, University of Bath, Bath, UK

Correspondence

Weiyou Yang, Institute of Micro/Nano Materials and Devices, Ningbo University of Technology, Ningbo, 315211 Zhejiang, People's Republic of China.

Email: weiyouyang@tsinghua.org.cn

Jie Teng, College of Materials Science and Engineering, Hunan University, 410082 Changsha, People's Republic of China. Email: tengjie@hnu.edu.cn

Funding information

Hunan Provincial Innovation Foundation for Postgraduate, Grant/Award Number: CX20200454; National Natural Science Foundation of China.

Grant/Award Number: 51972178

Abstract

We report the scalable fabrication of CdS/ZnS 1D/2D heterojunctions under ambient air conditions (i.e., room temperature and atmospheric pressure) in which ZnS nanoparticles are anchored on the surface of CdS nanosheets. The as-formed heterojunctions exhibit a significantly enhanced photocatalytic H₂ evolution rate of 14.02 mmol h⁻¹ g⁻¹ when irradiated with visible light, which is ~10 and 85 times higher than those of pristine CdS nanosheets and CdS nanoparticles, respectively, and superior to most of the CdS-based photocatalysts reported to date. Furthermore, they provide robust photocatalytic performance with demonstratable stability over 58 h, indicating their potential for practical applications. The formation of 1D/2D heterojunctions not only provides improved exposed active sites that respond to illumination but also provides a rapid pathway to generate photogenerated carriers for efficient separation and transfer through the matrix of single-crystalline CdS nanosheets. In addition, first-principles simulations demonstrate that the existence of rich Zn vacancies increases the energy level of the ZnS valence band maximum to construct type-II and Z-scheme mixed heterojunctions, which plays a critical role in suppressing the recombination of carriers with limited photocorrosion of CdS to enhance photocatalytic behavior.

KEYWORDS

air condition, CdS, heterojunctions, photocatalytic hydrogen production, ZnS

INTRODUCTION 1

Photocatalytic hydrogen evolution from water splitting is emerging as an attractive approach for exploring clean energy, 1-10 where one of the crucial challenges is to develop efficient and stable photocatalysts. 11-15 To date, there are

popular strategies to enhance the performance of photocatalysts: (i) creating blocks in a low-dimensional and single-crystalline configuration to facilitate the transport of photogenerated carriers^{16–21}; (ii) increasing the surface area to improve light harvesting and the number of active sites^{22–24}; (iii) constructing homo/heterojunctions for

This is an open access article under the terms of the Creative Commons Attribution License, which permits use, distribution and reproduction in any medium, provided the original work is properly cited.

© 2022 The Authors. Carbon Energy published by Wenzhou University and John Wiley & Sons Australia, Ltd.

Carbon Energy. 2022;1-14. wileyonlinelibrary.com/journal/cey2

26379368, 0, Downloaded from https://onlinelibrary.wiley.com/doi/10.1002/cey2.277 by Egyptian National Sti. Network (Enstinet), Wiley Online Library on [12/03/2023], See the Terms and Conditions (https://onlinelibrary.wiley.com/nerms

conditions) on Wiley Online Library for rules of use; OA articles are governed by the applicable Creative Commons License

energy band engineering to strengthen light absorption and charge separation efficiency. 25-31 Although the well-known type-I/-II heterojunctions are effective in improving photocatalytic activity, the redox ability of transferred electrons and holes is often weakened due to the release of partial potential energy, which is unfavorable for hydrogen production.^{32,33} In comparison, the formation of a Zscheme heterojunction not only promotes the separation of photo-induced carriers but maintains the redox capability to enhance photocatalytic hydrogen generation, 34-37 which has, therefore, been recognized as an effective technique for exploring advanced photocatalysts.

Among the family of semiconductor photocatalysts, cadmium sulfide (CdS) is an intriguing n-type semiconductor for photocatalytic H₂ production due to its relatively narrow band gap ($E_g \sim 2.4 \,\mathrm{eV}$), which can be highly active for harvesting visible light. 38-41 As a result, a number of strategies have been explored for growing CdS and CdS-based nanostructures, including hydrothermal, 42-44 solvothermal, 45-47 template, 48 and chemical deposition⁴⁹ methods, along with other techniques.^{50–52} Of particular note is that the majority of the reported works to date have often used high processing temperatures and pressures, organic/toxic reagents, and involved a time-consuming process.

Here, we report the kilogram-scale production of CdS nanosheets (CdS NSs)/ZnS nanoparticles (ZnS NPs) as 1D/ 2D heterojunctions (CdS-NSs/ZnS-NPs) under ambient air condition (room temperature [RT] and atmospheric pressure) based on a sonochemical strategy. The as-fabricated photocatalysts with rationally designed structures exhibit a significantly enhanced photocatalytic H2 evolution rate of 14.02 mmol h⁻¹ g⁻¹ when irradiated with visible light ($\lambda > 400$ nm), which is ~10 and ~85 times higher than those of pristine CdS NSs and CdS nanoparticles (CdS NPs), respectively. Furthermore, they exhibit highly stable photocatalytic behavior for over 58 h with an internal quantum yield of 2.76% when irradiated with 400 nm light, thereby demonstrating their potential as highly efficient and stable photocatalysts for practical applications. The mechanism for the enhanced photocatalytic activities of as-formed CdS-NSs/ ZnS-NPs type-II and Z-scheme mixed 1D/2D heterojunctions is also proposed based on first-principles simulations.

EXPERIMENTAL SECTION

Materials 2.1

The source materials of zinc acetate dihydrate (Zn (Ac)₂·2H₂O), sodium sulfide (Na₂S·9H₂O), cadmium chloride hydrate (CdCl₂·2.5H₂O), thiourea (CH₄N₂S), and sodium sulfite (Na₂SO₃) were obtained from Sigma-Aldrich.

Ethylenediamine (EDA) was obtained from Sinopharm Chemical Reagent Co., Ltd. Deionized water (DI H₂O) was used for all experiments. All reagents were used in asreceived conditions without further purification.

2.2 Sonochemical synthesis of ZnS NPs

For the fabrication of ZnS NPs based on the sonochemical method under ambient air conditions (i.e., RT and atmospheric pressure), in a typical process, 1 mmol Zn (Ac)2·2H2O with 1 mmol Na2S·9H2O was dissolved in 15 mL DI H₂O to form a white slurry solution while magnetic stirring at RT. The obtained solution was subjected to ultrasonic treatment at a frequency of 40 kHz for 30 min, followed by naturally cooling to RT. Subsequently, the ZnS NPs product was obtained by centrifugation and washed three times with DI H2O and ethanol, followed by freeze-drying overnight.

2.3 Sonochemical synthesis of CdS NPs

For fabrication of CdS NPs based on the sonochemical method under ambient air conditions, in a typical process, 1 mmol CdCl₂·2.5H₂O and 1 mmol Na₂S·9H₂O were dissolved in 15 mL DI H₂O to form an orange solution while magnetic stirring condition at RT. The obtained solution was then subject to ultrasonic treatment at a frequency of 40 kHz for 120 min, followed by naturally cooling to RT. Finally, the orange precipitates of CdS NPs were obtained by centrifugation and washing three times with DI H₂O and ethanol, followed by freeze-drying overnight.

Sonochemical synthesis of CdS NSs 2.4

For the fabrication of CdS NSs based on the sonochemical method under ambient air conditions, in a typical procedure, 5 mmol of CdCl₂·2.5H₂O and 15 mmol of CH₄N₂S were dissolved in 10 mL of ethylenediamine and 5 mL DI H₂O, which were subjected to ultrasonic treatment at a frequency of 40 kHz for 120 min, followed by naturally cooling to RT. Finally, the yellow precipitate of CdS NSs was obtained by centrifugation and washing three times with DI H₂O and ethanol, followed by freeze-drying overnight.

Sonochemical synthesis of CdS-2.5 NSs/ZnS-NPs heterojunctions

As for the fabrication of CdS-NSs/ZnS-NPs heterojunctions based on the sonochemical method under air conditions, in a typical process, 1.0 mmol as-prepared CdS NSs, different amounts of $Zn(Ac)_2 \cdot 2H_2O$ (0.2, 0.4, 0.6, 0.8, and 1.0 mmol) and $Na_2S \cdot 9H_2O$ (the molar ratio of Zn (Ac) $_2 \cdot 2H_2O$ to Na_2S was kept at 1, and the corresponding samples were labeled as CdS-NSs/ZnS-NPs-0.2, CdS-NSs/ZnS-NPs-0.4, CdS-NSs/ZnS-NPs-0.6, CdS-NSs/ZnS-NPs-0.8, and CdS-NSs/ZnS-NPs-1.0, respectively) were dispersed into 15 mL DI H_2O under magnetic stirring, which was subjected to ultrasonic treatment at a frequency of $40 \, \text{kHz}$ for $30 \, \text{min}$, followed by naturally cooling to RT. Finally, the product CdS-NSs/ZnS-NPs heterojunctions were collected by centrifugation and washed three times with DI H_2O and ethanol, followed by freeze-drying overnight.

2.6 | Kilogram-scale synthesis of CdS-NSs/ZnS-NPs heterojunctions

To demonstrate the capacity of kilogram-scale fabrication of CdS-NSs/ZnS-NPs heterojunctions, first, the source materials were extended up to 200 mmol (45.76 g) of CdCl₂·2.5H₂O and 200 mmol (45.76 g) of CH₄N₂S, which were dissolved in 400 mL of ethylenediamine and 200 mL DI H₂O. They were then mixed together and subjected to ultrasonic treatment at a frequency of 40kHz for 120 min, followed by naturally cooling to RT. Finally, a yellow precipitate was obtained by centrifugation and washing three times with DI H₂O and ethanol, followed by freezedrying overnight for the large-scale fabrication of CdS NSs. Second, the as-prepared CdS NSs with Zn (Ac)₂·2H₂O and Na₂S·9H₂O (the molar ratio of CdS $NSs:Zn(Ac)_2 \cdot 2H_2O:Na_2S = 0.6:1:1)$ were dispersed into 500 mL DI H₂O while magnetic stirring and subjected to ultrasonic treatment at a frequency of 40 kHz for 30 min, followed by naturally cooling to RT. Finally, the CdS-NSs/ZnS-NPs heterojunctions were collected by centrifugation and washing three times with DI H₂O and ethanol, followed by freeze-drying overnight. Similar experiments were repeated five times, leading to the fabrication 102.45 g CdS-NSs/ZnS-NPs of heterojunctions.

2.7 | Characterizations

Powder X-ray diffraction (PXRD; D8 Advance; Bruker) was utilized to evaluate the phase compositions under Cu $K\alpha$ X-ray radiation ($\lambda = 1.5406$ Å). The microstructure and morphology of as-prepared samples were observed under a field emission scanning electron microscope (FESEM; S-4800; Hitachi) and high-resolution transmission electron microscopy (HRTEM; JEM-2100F; JEOL) equipped with

energy dispersive X-ray spectroscopy (EDX; Quantax-STEM; Bruker). The compositions and valence band of the product were analyzed by X-ray photoelectron spectroscopy (XPS; Scientific K-Alpha; Thermo Fisher Scientific) with a reference of C 1s peak at 284.6 eV. The UV-Vis absorption spectrum was recorded on a UV-Vis scanning spectrophotometer (U-3900; Hitachi). Electron paramagnetic resonance (EPR) was conducted on a spectrometer (Bruker A300) at RT, while the radicals were captured by 5,5-dimethyl-1-pyrroline N-oxide (DMPO) under Xe lamp irradiation. The photoluminescence (PL) and timeresolved photoluminescence (TRPL) spectra were tested on a spectrometer (FLS-1000; Edinburgh) excited at 380 nm. The porous properties of as-prepared samples were characterized using N2 adsorption at 77 K on a specific surface area and porosity analyzer (Micromeritics; ASAP 2020 M).

2.8 | Photocatalytic hydrogen evolution

The analyses on the photocatalytic H₂ evolution of the asfabricated samples were performed on a top-irradiation quartz cell connected to a photocatalytic H2 evolution system (CEL-SPH2N). In a typical experiment, 10 mg of the as-prepared sample was suspended in 100 mL of distilled water containing 0.25 M sodium sulfite (Na₂SO₃) and 0.35 M sodium sulfide (Na₂S) as sacrificial agents. Before the irradiation, the reactant system was degassed by evacuation to remove the air, which ensured that the reaction system was under anaerobic conditions. After that, the system was irradiated by a 300-W Xe lamp with a cutoff filter of 400 nm for H2 evolution under magnetic stirring conditions. A thermal conductivity detector gas phase chromatograph (GC-7920) was employed to determine the amount of H2 evolution with the carrier gas of nitrogen (N2). Over the photocatalytic reaction, the temperature was maintained at 6°C by a flow of cooling water.

2.9 | Photoelectrochemical (PEC) measurement

PEC measurements were performed on an electrochemical analyzer (Chenhua CHI 660D) in a standard three-electrode cell with photocatalyst-coated fluorine-doped tin oxide (FTO) as the working electrode (active area: ~1 cm²), Ag/AgCl as the reference electrode, and a Pt plate as the counter electrode. A 300 W Xe lamp with a cut-off filter (λ > 400 nm) was used as the light source, and the Na₂SO₄ (0.5 M, pH = 6.8) aqueous solution was used as a supporting electrolyte. The working electrodes

26379368, 0, Downloaded from https://onlinelibrary.wiley.com/doi/10.1002/cey2.277 by Egyptian National Sti. Network (Enstinet), Wiley Online Library on [12032023]. See the Terms and Conditions (https://onlinelibrary.wiley.com/erms

and-conditions) on Wiley Online Library for rules of use; OA articles are governed by the applicable Creative Commons License

were prepared by dropping a suspension (20 µL) made of samples ZnS NPs, CdS NSs, and CdS NSs/ZnS-NPs-0.6 with a given concentration of 5 mg mL⁻¹ onto the surface of a precleaned FTO plate, followed by drying in air at RT. The Mott-Schottky (MS) curves were measured in the dark at a frequency of 0.5, 1.0, and 2.0 kHz, respectively. Transient photocurrent measurements (achieved by light on and off alternating every 5s) were recorded under visible light irradiation, with an optical cutoff filter of 400 nm installed on a 300 W Xe lamp for visible light excitation. Electrochemical impedance spectra (EIS) were collected at an off-line potential with frequencies ranging from 100 kHz to 0.1 Hz and modulation amplitude of 5.0 mV. The measured potentials (V vs. Ag/AgCl) were converted to the normal hydrogen electrode (NHE) scale according to the Nernst equation: E(NHE) = E(Ag/AgCl) + 0.197. In addition, the apparent quantum yield (AQY) was measured under the same photocatalytic reaction conditions with different single wavelengths of 400, 420, 450, and 520 nm band-pass filters. The AQY was calculated using the following equation:

$$AQY$$
 (%) = $\frac{\text{Number of evolved hydrogen atoms }(N_{\text{H}})}{\text{Number of incident photons }(N_{\text{P}})} \times 100$, $N_{\text{P}} \frac{A \times I}{E} \times t = \frac{A \times I}{(hc/\lambda)} \times t$, $N_{\text{H}} = 2 \times n_{H_2} \times N_A$,

where n_{H_2} is the moles of evolved hydrogen molecular, N_A is the Avogadro constant (6.02 × 10²³ mol⁻¹), I is the light intensity at 400, 420, 450 and 520 nm, A is the illuminated area, E is the photon energy, h is the Planck constant $(6.63 \times 10^{-34} \,\mathrm{J \, s})$, and c is the light rate $(3 \times 10^8 \, \text{m/s}).$

2.10 | Density functional theory (DFT) calculations

To investigate the band structures of ZnS and CdS in the heterojunctions, we performed ab initio calculations employing DFT, as implemented in Vienna Abinitio Simulation Package,⁵⁴ which was based on the projector-augmented wave potentials.⁵⁵ The energy cutoff of 400 eV was used for plane-wave expansion of electron wave functions based on the convergence test. The generalized gradient approximation with the Perdew Burke Ernzerhof functional was chosen to examine the exchange-correlation potential.⁵³ The following valence electron configurations are used: $4s^23d^{10}$ of Zn, $5s^24d^{10}$ of Cd, $3s^23p^4$ of S. For ZnS/CdS heterojunctions, they were composed of a ZnS (111) surface and a CdS (002) surface with a lattice mismatch smaller than 5%. To prevent unphysical

charge transfer between the top and bottom slab surfaces, pseudohydrogens with fractional charges were used to saturate the dangling bonds of Cd atoms at the bottom and S atoms on the top of the heterojunctions. A 15-Å-thick vacuum layer was used for all the surfaces to isolate the slabs. A $4 \times 4 \times 1$ Γ centered k-points mesh was used for the sampling of Brillouin zone integration in the calculation of ZnS/CdS heterojunctions. We also built a neutral Zn vacancy (V_{Zn}) in the interface of ZnS/CdS heterojunctions to investigate the influence of $V_{\rm Zn}$ on the band structures. All ZnS/CdS heterojunctions were fully relaxed in structure optimization with an energy convergence tolerance of 1.0×10^{-4} eV/atom and a maximum force less than 0.05 eV/Å.

The surface energy was determined by the slab calculations:

$$\sigma = (E_{\text{slab}} - nE_{\text{bulk}})/2A$$
,

where E_{slab} , E_{bulk} , n, and A were referred to the total energies of unrelaxed slab model and bulk phase, the number of bulk phases in the slab model, and the surface area of the slab model, respectively.

3 RESULTS AND DISCUSSION

With regard to the growth of CdS nanosheets (CdS NSs), CdCl₂·2.5H₂O precursors with different sulfur sources are introduced into the solvent and then subjected to ultrasonic treatment at air conditions, namely, at RT and atmospheric pressure (see the details in Section 2). Notably, when using $H_2O + Na_2S$ as the sulfur source, only CdS nanoparticles (CdS NPs) could be grown (Figure S1). Interestingly, when using $EDA + H_2O +$ CH₄N₂S as the sulfur source, the growth of CdS NSs is accomplished, implying that the growth of CdS nanostructures is tunable in terms of morphology, which is primarily attributed to the difference in polarity between H₂O and EDA. To demonstrate the detailed growth of CdS NSs with a volume ratio of H_2O : EDA = 2:1 as the source materials, the time-dependent evolution of Cd NSs at fixed sonication times from 0.5 to 2 h with an interval of 0.5 h is recorded, as shown in Figure 1A-D. It is seen that, for a sonication time of 0.5 h, numerous fine-scale CdS NPs are formed, as shown in Figure 1A. However, when the reaction time is extended to 1 h, thin CdS NSs are formed (Figure 1B). On further increasing the reaction time to 1.5 h, the CdS NSs grow continuously, as outlined in Figure 1C. Finally, for a reaction time of 2 h, a flower-like configuration is produced (see Figure 1D and Figure S2). In summary, as schematically shown in Figure 1E, the

26379368, 0, Downloaded from https://onlinelibrary.wiley.com/doi/10.1002/cey2.277 by Egyptian National Sti. Network (Enstinet), Wiley Online Library on [12/03/2023]. See the Terms

and Conditions (https://onlin

ditions) on Wiley Online Library for rules of use; OA articles are governed by the applicable Creative Commons

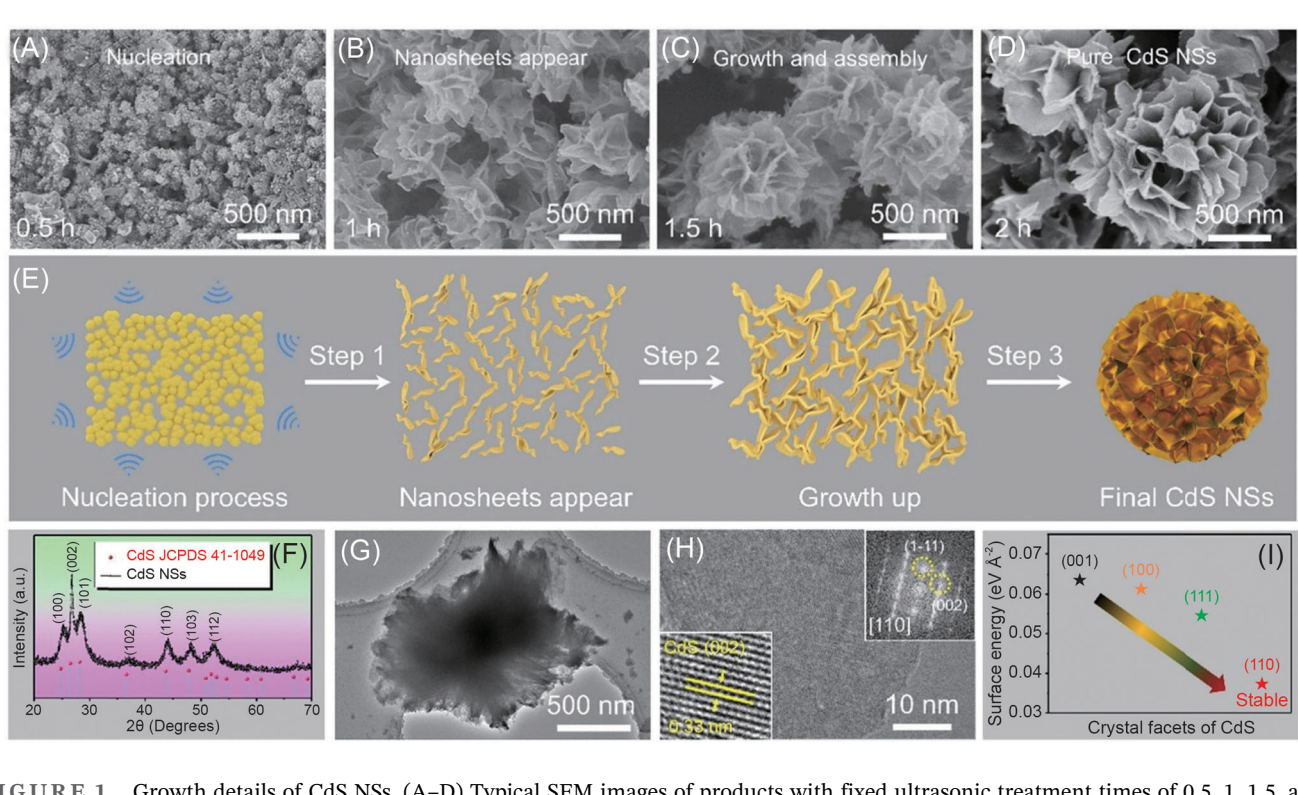


FIGURE 1 Growth details of CdS NSs. (A–D) Typical SEM images of products with fixed ultrasonic treatment times of 0.5, 1, 1.5, and 2 h, respectively. (E) Schematic of the growth process of CdS NSs. (F) XRD pattern of pure CdS NSs. (G,H) TEM and HRTEM images of CdS NSs, respectively. Inset in (H) is the corresponding FFT pattern. (I) DFT calculations of the surface energies of CdS. DFT, density functional theory; FFT, fast Fourier transition; HRTEM, high-resolution transmission electron microscopy; NS, nanosheet; SEM, scanning electron microscopy; TEM, transmission electron microscopy; XRD, X-ray diffraction.

growth of CdS NSs involves three primary stages, namely (i) the nucleation of CdS NSs (Step 1 in Figure 1E), (ii) the continued growth of CdS NSs (Step 2 in Figure 1E), and (iii) final assembly into a flower-like configuration (Step 3 in Figure 1E). Figure 1F provides a typical XRD pattern, showing their pure hexagonal crystal structure (JCPDS Card No. 41-1409). Figure 1G and Figure S3 present typical transmission electron microscopy (TEM) images of as-synthesized CdS NSs, further demonstrating their typical flower-like shape morphology. HRTEM analysis in Figure 1H and fast Fourier transition (FFT) analysis (the inset of Figure 1H) of individual nanosheets indicate their single-crystalline nature with an exposed close-packed plane of (110).⁵⁶ According to our DFT calculation in Figure 1I, it is confirmed that the surface energy of the (110) plane is the most thermodynamically stable plane, which, therefore, leads to the formation of nanosheets rather than nanoparticles.⁵⁷

Figure 2A is a schematic of a typical process for fabricating CdS-nanosheets/ZnS-nanoparticles (CdS-NSs/ZnS-NPs) heterojunctions based on the sonochemical method under air conditions (i.e., RT and atmospheric pressure), of which the exact details are outlined in Section 2. The approach involves two main steps, namely, the initial growth of CdS NSs and subsequent growth of

ZnS NPs on the surface of CdS NSs, both of which are performed by a sonochemical process under ambient conditions. For performance comparison, pure ZnS NPs are also fabricated, and the details are described in Section 2 and Figure S4. As a representative sample, the CdS-NSs/ZnS-NPs-0.6 heterojunctions refer to the product formed using source materials of 1.0 mmol as-grown CdS NSs, 0.6 mmol Zn(Ac)₂·2H₂O and 0.6 mmol Na₂S·9H₂O, and the details are provided in Section 2. In contrast to the pure CdS NSs in Figure 1D, the nanosheet surfaces become rough, indicating the deposition of ZnS NPs onto the CdS NPs, as seen in Figure 2B,C and Figure S5. SEM images of the products incorporating a variety of ZnS NPs amounts of 0.2, 0.4, 0.8, and 1.0 mmol (referred to as samples CdS-NSs/ZnS-NPs-0.2, CdS-NSs/ZnS-NPs-0.4, CdS-NSs/ZnS-NPs-0.8 and CdS-NSs/ZnS-NPs-1.0, respectively) are presented in Figure S6. Figure 2D provides the XRD pattern of sample CdS-NSs/ZnS-NPs-0.6 heterojunctions, and the samples with other mole ratios of ZnS NPs are presented in Figure S7. It can be seen that strong diffractions from hexagonal CdS NSs appear in all samples (JCPDS Card No. 41-1049), with detectable diffractions from cubic ZnS, as indicated by the blue dotted lines in Figure 2D and Figure S8 (JCPDS Card No. 05-0566). 58,59 The XRD pattern of pure CdS NSs in Figure 1F also

26379368, 0, Downloaded from https://onlinelibrary.wiley.com/doi/10.1002/cey2.277 by Egyptian National Sti. Network (Enstinet), Wiley Online Library on [1203/2023]. See the Terms

on Wiley Online Library for rules

of use; OA articles are governed by the applicable Creative Commons

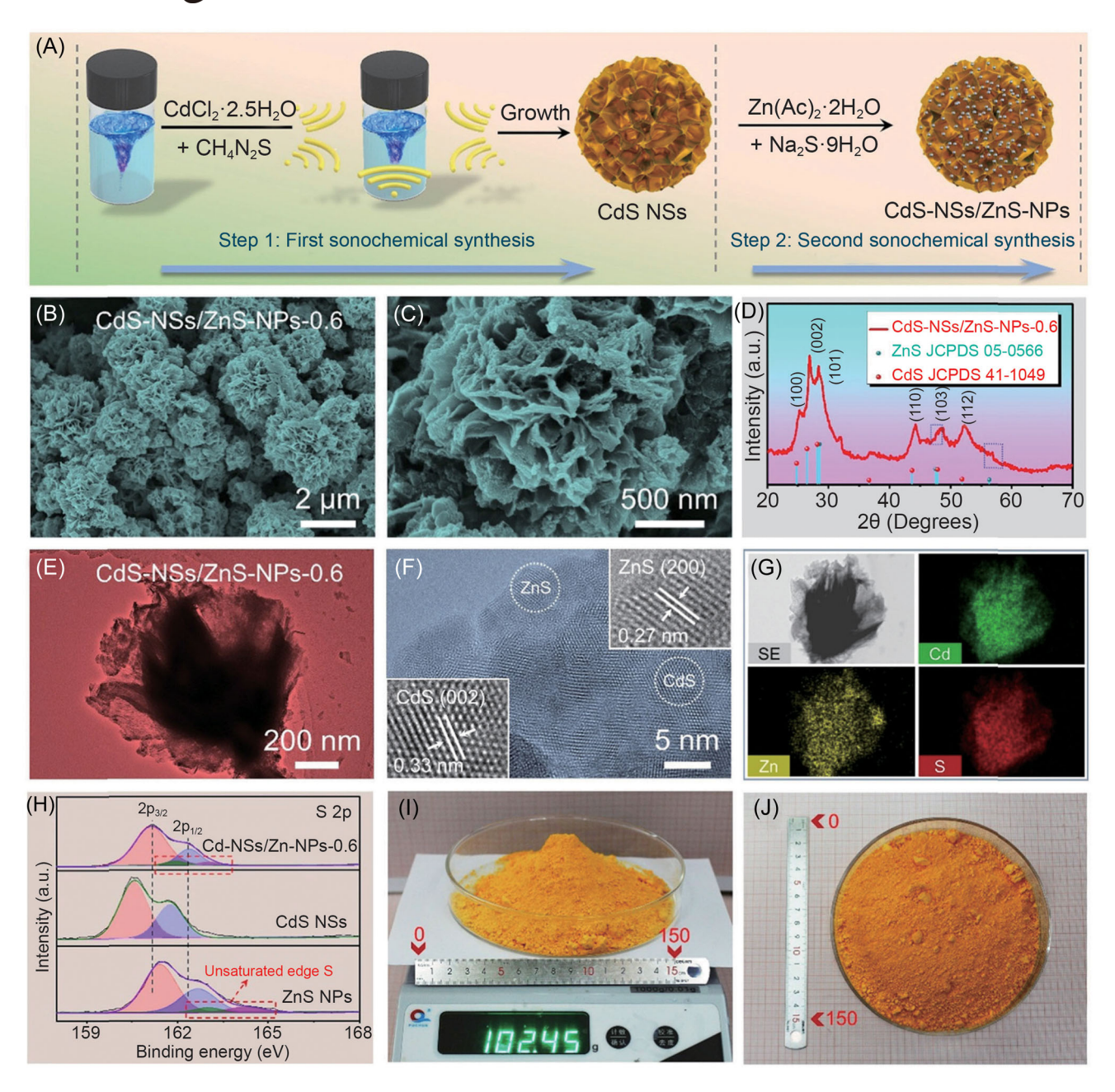


FIGURE 2 Fabrication and microstructural characterization of CdS-NSs/ZnS-NPs heterojunctions. (A) Schematic of the fabrication of CdS-NSs/ZnS-NPs heterojunctions. (B-G) Typical SEM images, XRD pattern, TEM, HRTEM, and element mappings images of sample CdS-NSs/ZnS-NPs-0.6. (H) High-resolution XPS spectra of S 2p of ZnS NPs, CdS NSs, and CdS-NSs/ZnS-NPs-0.6. (I,J) Digital photographs showing kilogram-scale production of CdS-NSs/ZnS-NPs heterojunctions. HRTEM, high-resolution transmission electron microscopy; NS, nanosheet; NPs, nanoparticles; SEM, scanning electron microscopy; TEM, transmission electron microscopy; XPS, X-ray photoelectron spectroscopy; XRD, X-ray diffraction.

indicates that the introduced ZnS has not affected the crystallinity of CdS, suggesting that the ZnS NPs are simply anchored onto the surface of CdS NSs. Figure 2E-F show the typical TEM and HRTEM images of CdS-NSs/ ZnS-NPs-0.6 heterojunctions, where the observed 0.27 nm lattice fringes are attributable to the (200) plane of cubic ZnS, while those with 0.33 nm fringes are indexed to the (002) plane of hexagonal CdS, in agreement with the XRD

characterization (Figure 1F and Figure S8). The corresponding EDX analyses are shown in Figure 2G and Figure S9, clarifying that it is mainly composed of Zn, Cd, and S. Moreover, the EDX characterization data demonstrate that the ZnS NPs have a uniform spatial distribution on the surface of CdS NSs, leading to the formation of 1D/ 2D heterojunctions. Furthermore, XPS analyses indicate the presence of unsaturated edge S atoms on the

surfaces of the CdS-NSs/ZnS-NPs-0.6 sample and ZnS NPs, as shown by the red dotted lines in Figure 2H.^{58,60} In comparison to the ZnS NPs, the high-resolution XPS spectrum of S 2p of pure ZnS has only two peaks at 161.75 and 162.93 eV (Figure S10A), which can be assigned to S $2p_{3/2}$ and S $2p_{1/2}$, respectively. The binding energies for Zn 2p_{3/2} and Zn 2p_{1/2} of pure ZnS observed at 1021.91 and 1045.01 eV (Figure S10B) have a shift of ~0.7 eV toward higher binding energy. The binding energies for Zn 2p and S 2p of ZnS NPs exhibit a shift to lower energy, as compared to pure ZnS, which can be attributed to the presence of rich defect states within the ZnS NPs. In such circumstances, a single negatively charged Zn vacancy is located near S2-, leading to an increase in the electron density around the Zn vacancy and a decrease in the binding energy of S²⁻. The XPS (Table S1) and inductively coupled plasma mass spectrometry (Table S2) analyses indicate that the ratio of Zn and S elements in the ZnS NPs is considerably lower than that in pure ZnS, also highlighting the presence of Zn defects in ZnS NPs. To obtain more information about the Zn vacancy defects, EPR measurement is also performed, and a very strong ESR signal at g = 2.007 was observed (Figure S11), which can be attributed to the presence of abundant Zn vacancies. In addition, the observed shifts of S 2p and Cd 3d within sample CdS-NSs/ZnS-NPs-0.6 suggest the presence of strong interactions among the CdS and ZnS (Figure 2H and Figure S12). Furthermore, as shown in Figure S13, the BET surface area of the CdS-NSs/ZnS-NPs-0.6 sample is fundamentally improved, in comparison to those of ZnS NPs samples, which is also beneficial to increasing the photocatalytic hydrogen reactive sites. To show the potential for mass production of CdS-NSs/ ZnS-NPs-0.6 heterojunctions under ambient air conditions, the source materials of CdCl₂·2.5H₂O and CH₄N₂S extended in size up to 45.67 g the details in Section 2). Consequently, after a twostep sonication treatment, 102.45 g of CdS-NSs/ZnS-NPs-0.6 photocatalysts could be obtained, as shown in Figure 2I,J. It should be noted that their phase composition (Figure S14A) and morphology (Figure S14B) are well maintained, similar to those in Figures 2C and 2D, underscoring that the present strategy is simple, efficient, and appropriate for mass production of CdS-NSs/ZnS-NPs heterojunctions under air conditions. It is worth noting that the whole process for fabricating CdS/ZnS heterojunctions is performed under ambient air conditions, which excludes the assistance of externally applied high temperatures and high pressures, as required in most other work concerning the synthesis of CdS-based nanostructures reported to date.42-47

The photocatalytic hydrogen production activity of the as-synthesized products is characterized under visible light irradiation ($\lambda > 400 \text{ nm}$), as shown in Figure 3A. The results indicate that the pure CdS NSs deliver an H₂ evolution rate of 1.39 mmol h⁻¹ g⁻¹, which is approximately eight times higher than that of CdS NPs $(0.16 \text{ mmol h}^{-1} \text{ g}^{-1})$. The H₂ production efficiency of pure ZnS NPs under visible light is even lower at 0.12 mmol h⁻¹ g⁻¹. With respect to the CdS-NSs/ZnS-NPs heterojunctions, the H₂ evolution rates are ca. 3.79, 11.99, 14.02, 13.01, and $8.24 \,\mathrm{mmol}\,h^{-1}\,\mathrm{g}^{-1}$ for samples CdS-NSs/ZnS-NPs-0.2, CdS-NSs/ZnS-NPs-0.4, CdS-NSs/ZnS-NPs-0.6, CdS-NSs/ZnS-NPs-0.8, and CdS-NSs/ZnS-NPs-1.0, respectively, indicating that the highest rate of H₂ production is achieved once the introduced ZnS NPs are fixed at a molar ratio of 0.6. The optimized one of $14.02 \text{ mmol h}^{-1} \text{ g}^{-1}$ is ~10 and 85 times higher than those of pure CdS NSs (1.39 mmol h⁻¹ g⁻¹) and CdS NPs $(0.16 \text{ mmol h}^{-1} \text{ g}^{-1})$, respectively, superior to most of the CdS-based photocatalysts and other systems ever reported, as summarized in Figure 3B and Tables S3 and S4. 44,61-75 Moreover, as shown in Figure 3C, sample CdS-NSs/ZnS-NPs-0.6 exhibits a stable photocatalytic activity over four cycles for 12 h, suggesting excellent stability against H₂ production. Moreover, after a 12 h reaction time, its morphology (Figure S15A-C) and phase composition (Figure S15D) are almost the same as those before H₂ production, further reflecting its robust stability to be employed as a stable photocatalyst. More importantly, the long-term stability of sample CdS-NSs/ ZnS-NPs-0.6 for H₂ production demonstrates that the H₂ production rate is highly stable with 313.92 mmol g⁻¹ H₂ produced over 58 h of irradiation, as shown in Figure 3D. To evaluate the light harvest efficiency, the wavelength-dependent AQY of photocatalytic H2 evolution for CdS-NSs/ZnS-NPs-0.6 heterojunctions is calculated as ~2.76% at 400 nm (Figure 3E). The excellent photocatalytic performance can be assumed to be a consequence of the rationally designed CdS-NSs/ZnS-NPs 1D/2D heterojunctions in which not only both the CdS NSs and ZnS NPs have sufficient exposed active sites to respond to the illumination but also the matrix of single-crystalline CdS NSs can provide an ideal pathway for the separation and transfer of photogenerated carriers.

UV-Vis diffuse reflectance absorbance spectrum is performed to investigate the optical properties of the photocatalysts, as shown in Figure 4A. The corresponding Tauc plots are used to estimate their band gaps, as disclosed in Figure 4B. Both CdS NSs and CdS-NSs/ZnS-NPs-0.6 heterojunctions exhibit strong absorption over the region from UV to visible light, due to the relatively narrow band gaps of CdS ($E_{\rm g} \sim 2.41\,{\rm eV}$) and CdS-NSs/ZnS-NPs-0.6

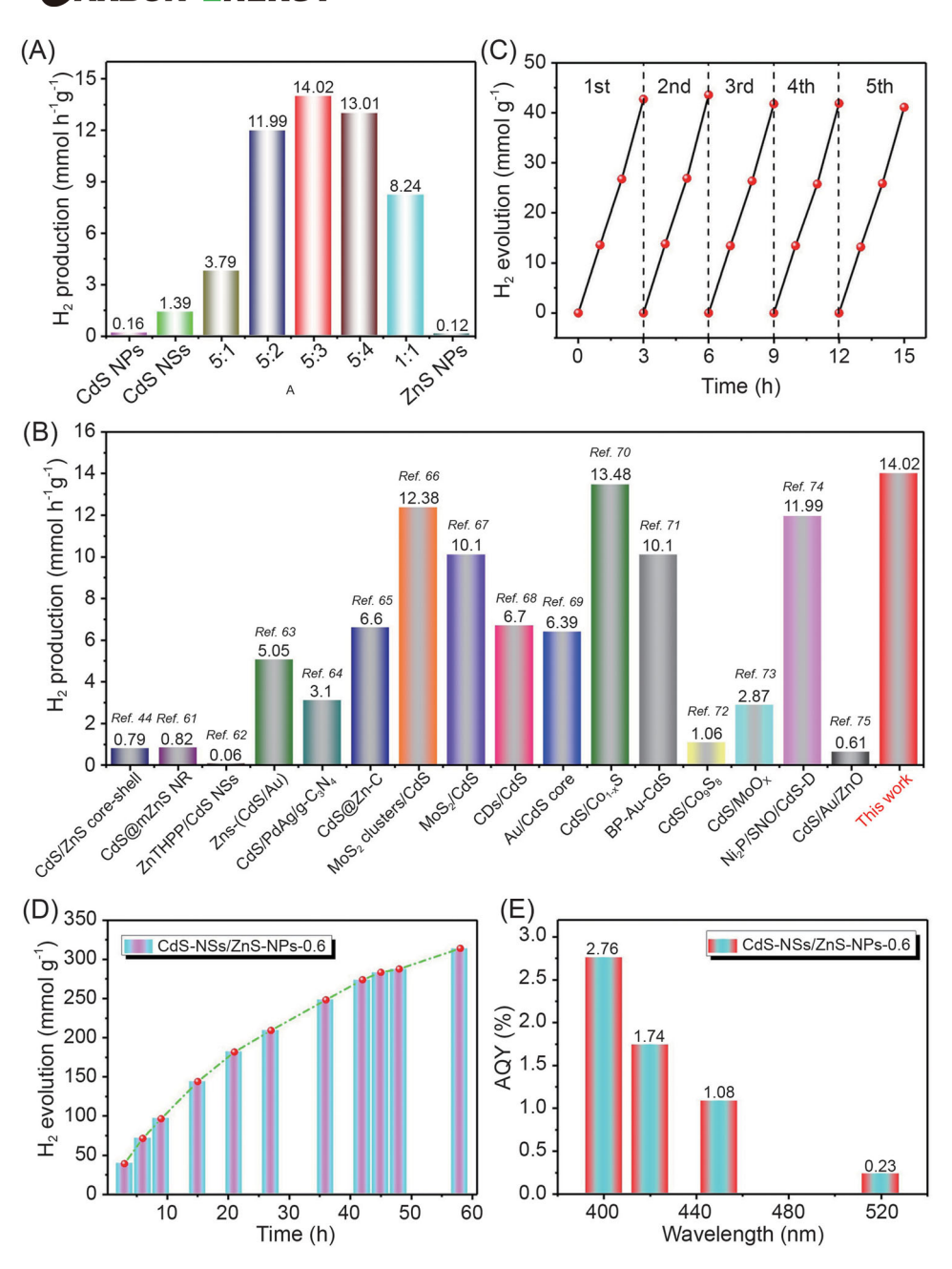


FIGURE 3 Visible-light-driven photocatalytic H₂ evolution performance. (A) Average photocatalytic H₂ evolution rates for different samples. (B) Typical H₂ evolution rates of CdS-based photocatalysts reported to date. (C) Photocatalytic stability of CdS-NSs/ZnS-NPs-0.6. (D) Long-term photocatalytic stability of sample CdS-NSs/ZnS-NPs-0.6 for 58 h. (E) Wavelength-dependent AQY of CdS-NSs/ZnS-NPs-0.6. AQY, apparent quantum yield; NP, nanoparticle; NS, nanosheet.

 $(E_{\rm g}\sim 2.44~{\rm eV}).^{76}$ In comparison, the ZnS NPs only exhibit relatively strong absorption over the UV region, as a result of their intrinsically wide band gap $(E_{\rm g}\sim 2.99~{\rm eV})$. Meanwhile, as shown in Figure 4C, the photocurrent density of CdS-NSs/ZnS-NPs-0.6 heterojunctions is higher than those of ZnS NPs and CdS NSs, indicating the significantly enhanced transfer and separation efficiencies of photogenerated charge carriers. According to the EIS measurements in Figure 4D, the CdS-NSs/ZnS-NPs-0.6 heterojunctions exhibit the smallest arc

size in comparison to those of CdS NSs and ZnS NPs, clarifying their smaller electron transport resistance and the formation of an intimate interface between CdS NSs and ZnS NPs. As shown in Figure 4E,F, the recorded MS plots reveal that the flat band ($E_{\rm FB}$) potential of ZnS NPs is $-0.77~{\rm eV}^{59,60}$ (vs. NHE, $E({\rm NHE}) = E({\rm Ag/AgCl}) + 0.197$), which is more negative than that of CdS NSs ($-0.55~{\rm eV}$ vs. NHE).² The flat band potential for CdS-NSs/ZnS-NPs-0.6 heterojunctions is estimated to be 0.66 eV (vs. NHE), as shown in Figure S16.

26379368, 0, Dow

ded from https://onlinelibrary.wiley.com/doi/10.1002/cey2.277 by Egyptian National Sti. Network (Enstinet), Wiley Online Library on [12/03/2023]. See

Wiley Online Library for rules of use; OA articles are governed by the applicable Creative Commons

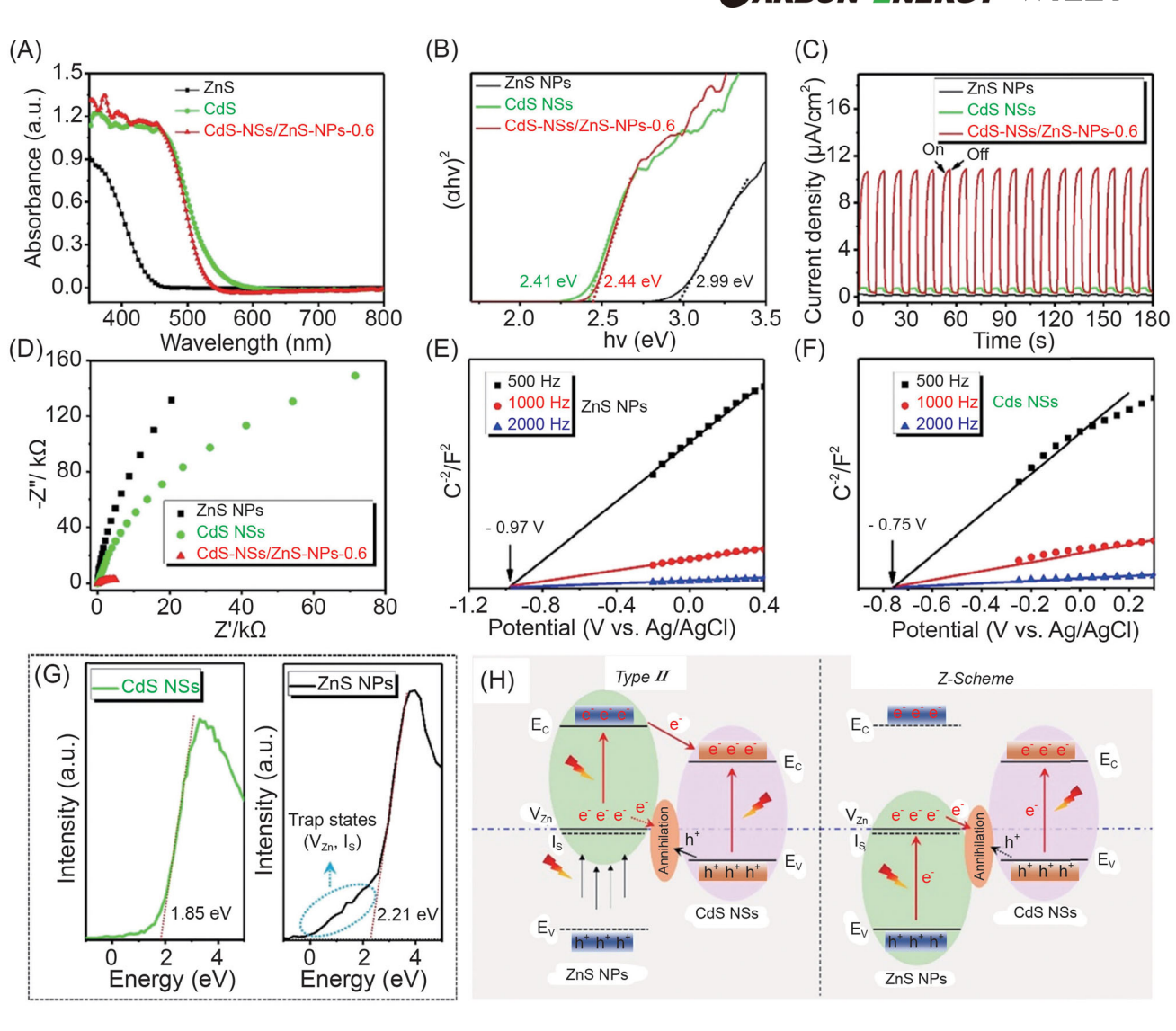


FIGURE 4 Mechanism of photocatalytic H₂ production. (A) UV-Vis diffuse reflectance spectra of a range of samples. (B) Calculated optical band gaps. (C) Transient photocurrent responses of a range of samples. (D) EIS of samples. (E,F) Mott–Schottky plots of ZnS NPs and CdS NSs, respectively. (G) VB XPS analysis of CdS and ZnS, showing the existence of trap states in ZnS. (H) Schematic of photocatalytic H₂ production over type-II and Z-scheme mixed CdS/ZnS heterojunction. EIS, electrochemical impedance spectra; NP, nanoparticle; NS, nanosheet; VB, valence band; XPS, X-ray photoelectron spectroscopy.

The shift of flat band potential witnesses the strong interaction among 1D ZnS NPs and 2D CdS NSs nanosheets, which favors the transfer of photogenerated carriers. It is known that, for n-type semiconductors, the position of the flat band potential is similar to that of the conduction band ($E_{\rm CB}$). Namely, the conduction bands of ZnS NPs and CdS NSs should be located at -0.77 and -0.55 eV, respectively. Accordingly, the valence band ($E_{\rm VB}$) of the ZnS NPs and CdS NSs can be calculated by $E_{\rm VB} = E_{\rm CB} + E_{\rm g}$, which are located at 2.22 and 1.86 eV, respectively, in agreement with the results of XPS VB spectra in Figure 4G. Furthermore, the XPS VB of the ZnS NPs shows the density of states within the valence band, in comparison with pure ZnS, as shown by the blue dotted lines in Figure 4G and Figure S17. These

results indicate the existence of trap states of $V_{\rm Zn}$ and $I_{\rm S}$ within the resultant heterojunctions, in agreement with the XPS and EPR analyses provided in Figure 2H and Figures S10 and S11. The separation and transfer processes of photogenerated charge carriers are investigated by the steady-state PL and TRPL spectroscopy, as shown in Figure S18. These results confirm that as-built CdS-NSs/ ZnS-NPs-0.6 heterojunction could suppress recombination of photo-induced charge carriers. Besides, the long-lived photogenerated electrons of NSs/ZnS-NPs-0.6 (17.06 ns) indicate that the charge recombination of CdS in the heterojunction is inhibited, implying that the transfer pathway hinders the recombination of charge carriers. Furthermore, in terms of the higher DMPO-OH intensity

26379368, 0, Downloaded from https://onlinelibrary.wiley.com/doi/10.1002/cey2.277 by Egyptian National Sti. Network (Enstinet), Wiley Online Library on [1203/2023]. See the Terms

Wiley Online Library for rules of use; OA articles are governed by the applicable Creative Commons

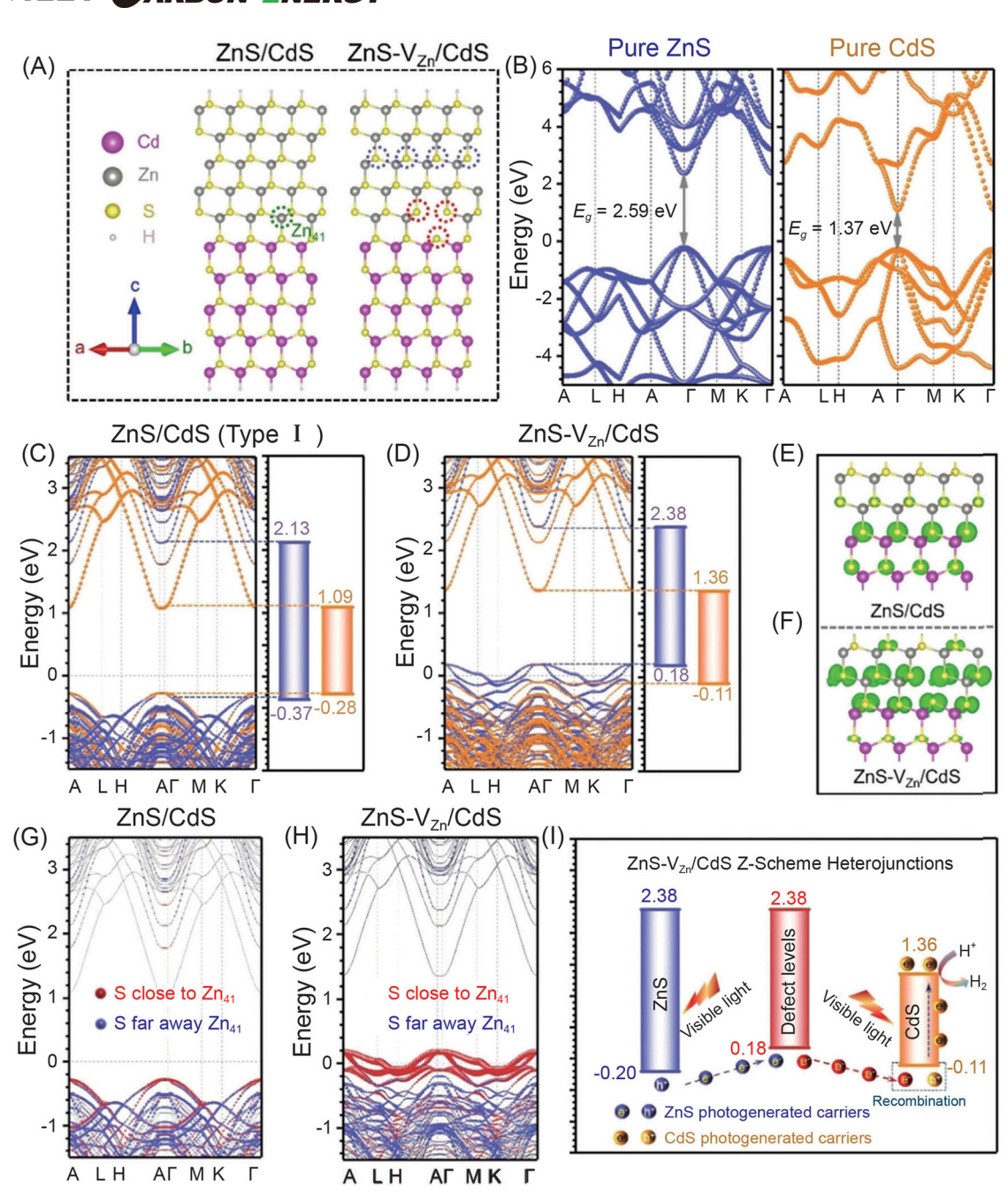


FIGURE 5 Theoretical investigation on photocatalytic H_2 production. (A) Crystal structures of ZnS/CdS heterostructure with and without Zn vacancy, with an example of Zn_{41} (the green, blue, and red dotted circle represents Zn atom No. 41 (labeled as Zn_{41}), S far away from Zn_{41} , and S close to Zn_{41} , respectively). (B) Energy band structures of pure ZnS (left) and CdS (right). (C,D) Energy band structures of ZnS/CdS heterostructure with and without Zn vacancy, respectively. The blue and yellow dotted regions represent the isolated ZnS and CdS band structures, respectively. (E,F) Partial charge densities at VBM of ZnS/CdS heterojunctions without and with V_{Zn} , respectively. (G,H) Contributions of S atoms close to and far away from Zn_{41} on the band structure of ZnS/CdS heterojunction with and without Zn vacancy, respectively. (I) Carrier transport within Z-scheme ZnS/CdS heterojunction. VBM, valence band maximum; V_{Zn} , Zn vacancy.

of CdS-NSs/ZnS-NPs-0.6 heterojunction (Figure S19), it suggests that the electron transfer mechanism does not follow the conventional type-I heterojunction mechanism. Based on the abovementioned analyses, the mechanism concerning the enhanced activity of photocatalytic $\rm H_2$ evolution is illustrated schematically in Figure 4H, and it

suggests that the improved photocatalytic performance primarily originates from the defect energy levels produced by Zn vacancies, which helps to build the desired type-II (the left part in Figure 4H) and Z-scheme (the right part in Figure 4H) mixed heterojunction. This facilitates an improved trapping capacity under visible light, with efficient

separation and transfer of photogenerated carriers. Consequently, the photogenerated electrons in the $E_{\rm CB}$ of CdS NSs is available to effectively reduce protons for producing H₂. Additionally, the high stability of the heterojunctions could be attributed to the fact that the photogenerated holes within CdS NSs is rapidly combined with electrons that exist within the defect levels of ZnS NPs, resulting in a suppressed holeled photocorrosion of CdS.

To provide a deeper insight into the electronic structure of as-fabricated CdS-NSs/ZnS-NPs heterojunctions, their bandgap alignments are theoretically investigated. In terms of the small lattice mismatch (<5%) between the ZnS (111) surface with/without $V_{\rm Zn}$ and CdS (002) surfaces, the ZnS/CdS heterojunction is constructed, as shown in Figure 5A. For comparison, the electronic structures of pure bulk ZnS and CdS are provided in Figure 5B. For the ZnS materials, it has a direct band gap of $E_{\rm g} \sim 2.59$ eV, with both the conduction band minimum (CBM) and valence band maximum (VBM) located at the Γ point. For CdS, it possesses a direct band gap of $E_g \sim 1.37 \,\text{eV}$ at Γ point. Figure 5C,D shows the band structures of ZnS/CdS heterojunctions without and with $V_{\rm Zn}$, respectively. It is observed that the electronic structures of both heterojunctions have a clean band gap, without midgap states. With respect to the condition without $V_{\rm Zn}$, once the $V_{\rm Zn}$ is introduced into the interface of heterojunction, as shown in the right part of Figure 5A, significant modification of the electronic structure occurs. This suggests that both the CBM and VBM of $ZnS-V_{Zn}$ are moved upward for the CdS component, inducing a change from a type-I heterojunction to a type-II one (the left part in Figure 4H). As a result, the photogenerated electrons of ZnS will be trapped in the defect levels, which is followed by recombination with the holes within the VB of CdS and partly transferred to the CB of CdS at the heterojunction interfaces. 44,77,78 Such a tailored band alignment would prevent the recombination of photogenerated carriers, facilitating a longer carrier lifetime to enhance photocatalytic behavior. Moreover, the partial charge densities at the VBM of ZnS/CdS without and with $V_{\rm Zn}$ are calculated, as shown in Figure 5E,F and Figure S20, which indicate the areas for generating photoinduced holes. In terms of the condition without V_{Zn} , the holes are located in the ZnS component. However, as shown by the movement of the charge density in the case with $V_{\rm Zn}$, the holes will transfer from CdS to ZnS components, indicating that the $V_{\rm Zn}$ could pull up the energy level of VBM of ZnS. In addition, the contributions of S atoms close to and far away from Zn₄₁ (as an example for Znvacancy defects in Figure 5A) in the band structure of ZnS/CdS without Zn vacancy are investigated, presenting that the electronic states of both type-S atoms are almost overlapped (Figure 5G). However, once the $V_{\rm Zn}$ is

generated at the Zn₄₁ site, an energy level split occurs, which makes the electronic states of the S atoms close to $V_{\rm Zn}$ for dominating the valence band edge (Figure 5H), which thus accounts for the upshift of VBM in ZnS. In terms of the breaking S–Zn bonds, the S atoms close to $V_{\rm Zn}$ become unsaturated, which is accompanied by the generation of dangling bonds around the VBM. Meanwhile, the electronic states of S atoms far away from the $V_{\rm Zn}$ are almost fixed due to the negligible effect of $V_{\rm Zn}$. As a result, the existence of V_{Zn} , as confirmed by the XPS analyses in Figure 2H, favors the formation of Z-scheme heterojunctions within sample CdS-NSs/ZnS-NPs, as schematically shown in Figure 5I and the right part in Figure 4H. As a result, the photogenerated electrons of bulk ZnS (the blue column in inset of Figure 51) will be trapped in the defect levels (the red line and column in Figures 5H and 5I, respectively), which is followed by recombination with holes within the VB of CdS at the heterojunction interfaces (the orange column in Figure 5I). In such a process, the electrons within the CB of CdS would be facilitated to participate in H₂ evolution reactions, favoring a limited photocorrosion of CdS. Overall, the enhanced spatial separation of photogenerated carriers induced by the constructed type-II and Z-scheme mixed 1D/2D heterojunctions plays a critical and important role in suppressing the recombination of charge carriers with limited photocorrosion of CdS, which thus leads to an enhanced photocatalytic behavior.

4 | CONCLUSION

In summary, we have demonstrated a sonochemistry strategy for kilogram-scale fabrication of CdS/ZnS 1D/2D heterojunctions under ambient air conditions (i.e., RT and atmospheric pressure), whereby uniformly distributed ZnS nanoparticles are anchored on the surface of CdS nanosheets. The resultant CdS-NSs/ZnS-NPs heterojunctions deliver a significantly enhanced photocatalytic H₂ evolution rate of 14.02 mmol h⁻¹ g⁻¹ under visible-light irradiation ($\lambda > 400 \text{ nm}$), which is ~10 and ~85 times higher than those of pristine CdS NSs and CdS NPs, respectively, and superior to most of the CdS-based photoanodes reported to date. Moreover, the heterojunctions provide excellent photocatalytic stability over 58 h, highlighting their potential for practical applications. The enhanced photocatalytic activity is attributed to the following key points: (i) the formed 1D/2D heterojunctions provide sufficient exposed active sites to respond to illumination by light and also provide a fast pathway for efficient separation and transfer of photogenerated carriers through the matrix of single-crystalline CdS NSs; (ii) the constructed type-II and Z-scheme mixed

heterojunctions are directed by the defect energy level of Zn vacancies, which increase the energy level of valence band maximum in ZnS. As a result, such heterojunctions play a critical role in suppressing the recombination of carriers with limited photocorrosion of CdS, thus enabling an enhanced photocatalytic behavior. The work has the potential to open a new door for large-scale production of advanced photocatalysts with rationally designed structures toward highly efficient and stable visible-light-driven photocatalytic H₂ evolution.

ACKNOWLEDGMENTS

This study was supported by the National Natural Science Foundation of China (grant no. 51972178) and Hunan Provincial Innovation Foundation for Postgraduate (grant no. CX20200454).

CONFLICT OF INTEREST

The authors declare no conflict of interests.

ORCID

Weiyou Yang http://orcid.org/0000-0002-3607-3514

REFERENCES

- 1. Han Z, Qiu F, Eisenberg R, Holland PL, Krauss TD. Robust photogeneration of H2 in water using semiconductor nanocrystals and a nickel catalyst. Science. 2012;338(6112): 1321-1324.
- 2. Wakerley DW, Kuehnel MF, Orchard KL, Ly KH, Rosser TE, Reisner E. Solar-driven reforming of lignocellulose to H₂ with a CdS/CdO_x photocatalyst. Nat Energy. 2017;2(4):17021.
- 3. Maeda K, Teramura K, Lu D, et al. Photocatalyst releasing hydrogen from water. Nature. 2006;440(7082):295.
- 4. Turner JA. Sustainable hydrogen production. Science. 2004; 305(5686):972-974.
- 5. Shi Y, Zhang B. Recent advances in transition metal phosphide nanomaterials: synthesis and applications in hydrogen evolution reaction. Chem Soc Rev. 2016;45(6): 1529-1541.
- 6. Li F, Yang H, Li W, Sun L. Device fabrication for water oxidation, hydrogen generation, and CO2 reduction via molecular engineering. Joule. 2018;2(1):36-60.
- 7. He K, Shen R, Hao L, et al. Advances in nanostructured silicon carbide photocatalysts. Acta Phys-Chim Sin. 2022;38(X):2201021.
- Bai J, Shen R, Jiang Z, Zhang P, Li Y, Li X. Integration of 2D layered CdS/WO₃ S-scheme heterojunctions and metallic Ti₃C₂ MXene-based Ohmic junctions for effective photocatalytic H₂ generation. Chinese J Catal. 2022;43(2):359-369.
- 9. Jiang X, Chen Y-X, Lu C-Z. Bio-inspired materials for photocatalytic hydrogen production. Chinese J Struc Chem. 2020;39(12):2123-2130.
- 10. Ma X-W, Lin H-F, Li Y-Y, et al. Dramatically enhanced visiblelight-responsive H2 evolution of Cd1-x Znx S via the synergistic effect of Ni₂P and 1T/2H MoS₂ cocatalysts. Chinese J Struc Chem. 2021;40(1):7-22.

- 11. Ma Y, Wang X, Jia Y, Chen X, Han H, Li C. Titanium dioxidebased nanomaterials for photocatalytic fuel generations. Chem Rev. 2014;114(19):9987-10043.
- 12. Liao L, Zhang Q, Su Z, et al. Efficient solar water-splitting using a nanocrystalline CoO photocatalyst. Nat Nanotechnol. 2013;9(1):69-73.
- 13. Fujishima A, Honda K. Electrochemical photolysis of water at a semiconductor electrode. Nature. 1972;238(5358):37-38.
- 14. Ma D, Shi J-W, Zou Y, Fan Z, Ji X, Niu C. Highly efficient photocatalyst based on a CdS quantum Dots/ZnO nanosheets 0D/2D heterojunction for hydrogen evolution from water splitting. ACS Appl Mater Interfaces. 2017;9(30): 25377-25386.
- 15. Li M-X, Guan R-Q, Li J-X, et al. Performance and mechanism research of Au-HSTiO2 on photocatalytic hydrogen production. Chinese J Struc Chem. 2020;39(8):1437-1443.
- 16. Wu L, Wang Q, Zhuang T-T, et al. Single crystalline quaternary sulfide nanobelts for efficient solar-to-hydrogen conversion. Nat Commun. 2020;11:5194.
- 17. Wang Q, Nakabayashi M, Hisatomi T, et al. Oxysulfide photocatalyst for visible-light-driven overall water splitting. Nat Mater. 2019;18(8):827-832.
- 18. Wang Z, Inoue Y, Hisatomi T, et al. Overall water splitting by Ta₃N₅ nanorod single crystals grown on the edges of KTaO₃ particles. Nat Catal. 2018;1(10):756-763.
- 19. Jiang Z, Chen Q, Zheng Q, Shen R, Zhang P, Li X. Constructing 1D/2D Schottky-Based heterojunctions between Mn_{0.2}Cd_{0.8}S nanorods and Ti₃C₂ nanosheets for boosted photocatalytic H₂ evolution. Acta Phys-Chim Sin. 2020;37(6):2010059.
- 20. Xiong Z, Hou Y, Yuan R, Ding Z, Ong WJ, Wang S. Hollow NiCo₂S₄ nanospheres as a cocatalyst to support ZnIn₂S₄ nanosheets for Visible-Light-Driven hydrogen production. Acta Phys-Chim Sin. 2021;38(7):2111021.
- 21. Ren D, Shen R, Jiang Z, Lu X, Li X. Highly efficient visiblelight photocatalytic H₂ evolution over 2D-2D CdS/Cu₇S₄ layered heterojunctions. Chin J Catal. 2020;41(1):31-40.
- 22. Sun Y, Sun Z, Gao S, et al. Fabrication of flexible and freestanding zinc chalcogenide single layers. Nat Commun. 2012;3:1057.
- 23. Zhao M, Wang Y, Ma Q, et al. Ultrathin 2D metal-organic framework nanosheets. Adv Mater. 2015;27(45):7372-7378.
- 24. Bai J, Shen R, Chen W, et al. Enhanced photocatalytic H₂ evolution based on a Ti₃C₂/Zn_{0.7}Cd_{0.3}S/Fe₂O₃ Ohmic/Sscheme hybrid heterojunction with cascade 2D coupling interfaces. Chem Eng J. 2022;429:132587.
- 25. Low J, Yu J, Jaroniec M, Wageh S, Al-Ghamdi AA. Heterojunction photocatalysts. Adv Mater. 2017;29(20):1601694.
- Zhao D, Wang Y, Dong C-L, et al. Boron-doped nitrogendeficient carbon nitride-based Z-scheme heterostructures for photocatalytic overall water splitting. Nat Energy. 2021;6(4): 388-397.
- 27. Kosco J, Bidwell M, Cha H, et al. Enhanced photocatalytic hydrogen evolution from organic semiconductor heterojunction nanoparticles. Nat Mater. 2020;19(5):559-565.
- 28. Liu S, Wang K, Yang M, Jin Z. Rationally designed Mn_{0.2}Cd_{0.8}S@CoAl LDH S-Scheme heterojunction for efficient photocatalytic hydrogen production. Acta Phys-Chim Sin. 2021;38(7):2109023.

- 29. Liu Y, Hao X, Hu H, Jin Z. High efficiency electron transfer realized over NiS₂/MoSe₂ S-Scheme heterojunction in photocatalytic hydrogen evolution. *Acta Phys-Chim Sin.* 2020; 37(6):2008030.
- 30. Bai J, Chen W, Shen R, et al. Regulating interfacial morphology and charge-carrier utilization of Ti₃C₂ modified all-sulfide CdS/ZnIn₂S₄ S-scheme heterojunctions for effective photocatalytic H₂ evolution. *J Mater Sci Technol*. 2022;112(10):85-95.
- 31. Li Y, Shen B, Li S, Zhao Y, Qu J, Liu L. Tracking S-scheme charge transfer pathways in Mo₂C/CdS H₂-evolution photocatalysts. *Solar RRL*. 2021;5(7):2100177.
- 32. Huang ZF, Song J, Wang X, et al. Switching charge transfer of $C_3N_4/W_{18}O_{49}$ from type-II to Z-scheme by interfacial band bending for highly efficient photocatalytic hydrogen evolution. *Nano Energy.* 2017;40:308-316.
- 33. Shen R, Ding Y, Li S, et al. Constructing low-cost Ni_3C /twin-crystal $Zn_{0.5}Cd_{0.5}S$ heterojunction/homojunction nanohybrids for efficient photocatalytic H_2 evolution. *Chin J Catal.* 2021;42(1):25-36.
- Xu H, She X, Fei T, et al. Metal-Oxide-Mediated subtractive manufacturing of two-dimensional carbon nitride for highefficiency and high-yield photocatalytic H₂ evolution. ACS Nano. 2019;13(10):11294-11302.
- 35. Wang X, Wang X, Huang J, Li S, Meng A, Li Z. Interfacial chemical bond and internal electric field modulated Z-scheme S_v-ZnIn₂S₄/MoSe₂ photocatalyst for efficient hydrogen evolution. *Nat Commun.* 2021;12:4112.
- Wang Y, Shang X, Shen J, et al. Direct and indirect Z-scheme heterostructure-coupled photosystem enabling cooperation of CO₂ reduction and H₂O oxidation. *Nat Commun.* 2020;11:3043.
- 37. Wang Q, Okunaka S, Tokudome H, et al. Printable photocatalyst sheets incorporating a transparent conductive mediator for Z-scheme water splitting. *Joule*. 2018;2(12):2667-2680.
- Han G, Jin Y-H, Burgess RA, Dickenson NE, Cao XM, Sun Y. Visible-light-driven valorization of biomass intermediates integrated with H₂ production catalyzed by ultrathin Ni/CdS nanosheets. J Am Chem Soc. 2017;139(44):15584-15587.
- Kudo A, Miseki Y. Heterogeneous photocatalyst materials for water splitting. *Chem Soc Rev.* 2009;38(1):253-278.
- 40. Zong X, Yan H, Wu G, et al. Enhancement of photocatalytic H_2 evolution on CdS by loading MoS_2 as cocatalyst under visible light irradiation. *J Am Chem Soc.* 2008;130(23): 7176-7177.
- 41. Cheng L, Xiang Q, Liao Y, Zhang H. CdS-based photocatalysts. Energy Environ Sci. 2018;11(6):1362-1391.
- 42. Tian L, Min S, Wang F. Integrating noble-metal-free metallic vanadium carbide cocatalyst with CdS for efficient visible-light-driven photocatalytic H₂ evolution. *Appl Catal B*. 2019;259(1):118029.
- 43. Hu Y, Hao X, Cui Z, et al. Enhanced photocarrier separation in conjugated polymer engineered CdS for direct Z-scheme photocatalytic hydrogen evolution. *Appl Catal B*. 2020;260:118131.
- 44. Xie YP, Yu ZB, Liu G, Ma XL, Cheng HM. CdS-mesoporous ZnS core-shell particles for efficient and stable photocatalytic hydrogen evolution under visible light. *Energy Environ Sci.* 2014;7(6):1895.

- 45. Utterback JK, Grennell AN, Wilker MB, Pearce OM, Eaves JD, Dukovic G. Observation of trapped-hole diffusion on the surfaces of CdS nanorods. *Nat Chem.* 2016;8(11):1061-1066.
- Robinson RD, Sadtler B, Demchenko DO, Erdonmez CK, Wang LW, Alivisatos AP. Spontaneous superlattice formation in nanorods through partial cation exchange. *Science*. 2007;317(5836):355-358.
- 47. Tseng H-W, Wilker MB, Damrauer NH, Dukovic G. Charge transfer dynamics between photoexcited CdS nanorods and mononuclear Ru water-oxidation catalysts. *J Am Chem Soc.* 2013;135(9):3383-3386.
- 48. Bao N, Shen L, Takata T, Domen K. Self-templated synthesis of nanoporous CdS nanostructures for highly efficient photocatalytic hydrogen production under visible light. *Chem Mater.* 2007;20(1):110-117.
- Sun Q, Wang N, Yu J, Yu JC. A hollow porous CdS photocatalyst. Adv Mater. 2018;30(45):1804368.
- 50. Duan X, Lieber CM. General synthesis of compound semiconductor nanowires. *Adv Mater.* 2000;12(4):298-302.
- 51. Zhu W, Liu X, Liu H, Tong D, Yang J, Peng J. Coaxial heterogeneous structure of TiO₂ nanotube arrays with CdS as a superthin coating synthesized via modified electrochemical atomic layer deposition. *J Am Chem Soc.* 2010;132(36): 12619-12626.
- 52. Ma D, Shi J-W, Sun L, et al. Knack behind the high performance CdS/ZnS-NiS nanocomposites: optimizing synergistic effect between cocatalyst and heterostructure for boosting hydrogen evolution. *Chem Eng J.* 2022;431:133446.
- 53. Perdew JP, Burke K, Ernzerhof M. Generalized gradient approximation made simple. *Phys Rev Lett.* 1996;77(18): 3865-3868.
- 54. Kresse G, Furthmuller J. Efficient iterative schemes for ab initio total-energy calculations using a plane-wave basis set. *Phys Rev B*. 1996;54(16):11169-11186.
- Kresse G, Joubert D. From ultrasoft pseudopotentials to the projector augmented-wave method. *Phys Rev B*. 1999;59(3): 1758-1775.
- 56. Liu F, Yan C, Huang J, et al. Nanoscale microstructure and chemistry of Cu₂ZnSnS₄/CdS interface in kesterite Cu₂ZnSnS₄Solar cells. *Adv Energy Mater*. 2016;6(15):1600706.
- Fan J, Zhao X, Mao X, et al. Large-area vertically aligned bismuthene nanosheet arrays from galvanic replacement reaction for efficient electrochemical CO₂ conversion. Adv Mater. 2021;33(35):2100910.
- 58. Yu K, Huang H-B, Wang J-T, et al. Engineering cation defect-mediated Z-scheme photocatalysts for a highly efficient and stable photocatalytic hydrogen production. *J Mater Chem A*. 2021;9(12):7759-7766.
- Xin Y, Huang Y, Lin K, Yu Y, Zhang B. Self-template synthesis
 of double-layered porous nanotubes with spatially separated
 photoredox surfaces for efficient photocatalytic hydrogen
 production. *Sci Bull.* 2018;63(10):601-608.
- Hao X, Wang Y, Zhou J, Cui Z, Wang Y, Zou Z. Zinc vacancypromoted photocatalytic activity and photostability of ZnS for efficient visible-light-driven hydrogen evolution. *Appl Catal B*. 2018;221:302-311.
- 61. Lian Z, Sakamoto M, Kobayashi Y, et al. Anomalous photoinduced hole transport in type I core/mesoporous-shell

- nanocrystals for efficient photocatalytic H_2 evolution. *ACS Nano.* 2019;13(7):8356-8363.
- 62. Ning X, Wu Y, Ma X, et al. A novel charge transfer channel to simultaneously enhance photocatalytic water splitting activity and stability of CdS. *Adv Funct Mater*. 2019;29(40):1902992.
- 63. Zhuang TT, Liu Y, Sun M, et al. A unique ternary semiconductor–(semiconductor/metal) nano-architecture for efficient photocatalytic hydrogen evolution. *Angew Chem Int Ed.* 2015;54(39):11495-11500.
- 64. Gao J, Zhang F, Xue H, et al. In-situ synthesis of novel ternary CdS/PdAg/g-C₃N₄ hybrid photocatalyst with significantly enhanced hydrogen production activity and catalytic mechanism exploration. *Appl Catal B*. 2021;281:119509.
- 65. Shi Y, Lei X, Xia L, Wu Q, Yao W. Enhanced photocatalytic hydrogen production activity of CdS coated with Zn-anchored carbon layer. *Chem Eng J.* 2020;393:124751.
- 66. Feng C, Chen Z, Hou J, et al. Effectively enhanced photocatalytic hydrogen production performance of one-pot synthesized MoS₂ clusters/CdS nanorod heterojunction material under visible light. Chem Eng J. 2018;345:404-413.
- 67. Chang K, Li M, Wang T, et al. Drastic layer-number-dependent activity enhancement in photocatalytic H₂ evolution over nMoS₂/CdS (n≥1) under visible light. *Adv Energy Mater*. 2015;5(10):1402279.
- 68. Zhu C, Liu C, Fu Y, et al. Construction of CDs/CdS photocatalysts for stable and efficient hydrogen production in water and seawater. *Appl Catal B.* 2019;242:178-185.
- 69. Xu J, Yang W-M, Huang S-J, et al. CdS core-Au plasmonic satellites nanostructure enhanced photocatalytic hydrogen evolution reaction. *Nano Energy*. 2018;49:363-371.
- Li L, Guo C, Shen J, Ning J, Zhong Y, Hu Y. Construction of sugar-gourd-shaped CdS/Co_{1-x}S hollow hetero-nanostructure as an efficient Z-scheme photocatalyst for hydrogen generation. *Chem Eng J.* 2020;400:125925.
- Cai X, Mao L, Yang S, Han K, Zhang J. Ultrafast charge separation for full solar spectrum-activated photocatalytic H₂ generation in a black phosphorus–Au–CdS heterostructure. ACS Energy Lett. 2018;3(4):932-939.
- 72. Qiu B, Zhu Q, Du M, Fan L, Xing M, Zhang J. Efficient solar light harvesting CdS/Co₉S₈ hollow cubes for Z-scheme photocatalytic water splitting. *Angew Chem Int Ed.* 2017;56(10):2684-2688.

- 73. Zhang H, Zhang P, Qiu M, Dong J, Zhang Y, Lou XW. Ultrasmall MoO_x clusters as a novel cocatalyst for photocatalytic hydrogen evolution. *Adv Mater.* 2018;31(6):1804883.
- Hu T, Dai K, Zhang J, Chen S. Noble-metal-free Ni₂P modified step-scheme SnNb₂O₆/CdS-diethylenetriamine for photocatalytic hydrogen production under broadband light irradiation. *Appl Catal B.* 2020;269:118844.
- Liu R, Wang LB, Huang RL, et al. Self-assembled CdS/Au/ ZnO heterostructure induced by surface polar charges for efficient photocatalytic hydrogen evolution. *J Mater Chem A*. 2013;1(8):2773-2841.
- Fan X-B, Yu S, Wu H-L, et al. Direct synthesis of sulfide capped CdS and CdS/ZnS colloidal nanocrystals for efficient hydrogen evolution under visible light irradiation. *J Mater Chem A*. 2018;6(34):16328-16332.
- Sun G, Shi J-W, Mao S, et al. Dodecylamine coordinated triarm CdS nanorod wrapped in intermittent ZnS shell for greatly improved photocatalytic H₂ evolution. *Chem Eng J*. 2022;429:132382.
- Ma D, Shi J-W, Zou Y, et al. Rational design of CdS@ZnO core-shell structure via atomic layer deposition for drastically enhanced photocatalytic H₂ evolution with excellent photostability. *Nano Energy*. 2017;39:183-191.

SUPPORTING INFORMATION

Additional supporting information can be found online in the Supporting Information section at the end of this article.

How to cite this article: Zhang D, Teng J, Yang H, et al. Air-condition process for scalable fabrication of CdS/ZnS 1D/2D heterojunctions toward efficient and stable photocatalytic hydrogen production. *Carbon Energy*. 2022;1-14. doi:10.1002/cey2.277